

Composites Based on MIL-100(Fe) and Diatomite for the Photo-Fenton Degradation of Phenol

P. A. Matskan^{a,*}, E. V. Evdokimova^a, and G. V. Mamontov^a

^a National Research Tomsk State University, Tomsk, 634050 Russia

*e-mail: pmackan2002@gmail.com

Received December 26, 2022; revised February 15, 2023; accepted February 28, 2023

Abstract—Porous composites based on a MIL-100(Fe) metal–organic framework and a natural diatomite material have been synthesized. The composites are characterized by a specific surface area of 322 and 441 m²/g and a hierarchical pore structure represented by wide pores of the original diatomite and narrow meso- and micropores of the formed MIL-100(Fe) particles. The effect of synthesis approach on the structure of the composites and their catalytic properties in the photocatalytic degradation of phenol has been studied. In the composite synthesized with the preimpregnation of diatomite with an iron nitrate solution, MIL-100(Fe) particles are mostly formed inside the diatomite pores. The composite samples exhibit catalytic activity in the photo-Fenton degradation of phenol. The highest activity is exhibited by the sample synthesized without any preimpregnation of diatomite; this sample is characterized by the dominant formation of MIL-100(Fe) particles on the external surface of the diatomite.

Keywords: MIL-100(Fe), diatomite, hierarchical structure, heterogeneous photo-Fenton, phenol

DOI: 10.1134/S0023158423040067

INTRODUCTION

The wastewater of oil refineries; coking and petrochemical plants; and enterprises of the pharmaceutical, plastic, woodworking, paint-and-varnish, and pulp-and-paper industries contains phenols, which are highly toxic compounds. The discharge of phenol-containing water into open water bodies can entail deplorable consequences; therefore, water is purified from phenols using activated carbon adsorption, extraction with nonpolar solvents, purification with ion-exchange resins, and other approaches [1].

One of the most effective wastewater treatment methods is the degradation of pollutants with hydrogen peroxide. The oxidation of organic compounds in the presence exclusively of H₂O₂ occurs slowly; however, the addition of transition metal salts, which typically contain iron ions, leads to a significant acceleration of the process. This reaction is referred to as the Fenton reaction. Advantages of using the Fenton reaction are the high efficiency for the degradation of organic compounds and the cost effectiveness of this method. However, this approach is not free of disad-

vantages: it is a homogeneous catalytic process; accordingly, the separation of the catalyst from the reaction mixture is hindered; in addition, the pH range providing the stability and activity of the catalytic system is limited [2]. The use of heterogeneous Fenton catalysts contributes to the elimination of the above problems [3]. A supplementary exposure of semiconductor catalysts to light initiates the photo-Fenton process, which accelerates the degradation of organic pollutants.

In this study, a MIL-100(Fe) metal–organic framework (MOF) composed of iron oxide clusters and trimesic acid (BTC) was used as a heterogeneous catalyst for phenol oxidation via the Fenton reaction [4]. The MIL-100(Fe) MOF can be involved in the photo-Fenton process due to the presence of FeO_x clusters in the structure; these clusters effectively absorb visible light owing to the tendency to generating photogenerated electrons and holes [5]. Metal–organic frameworks have a large surface area and, accordingly, a high sorption capacity. However, the microporous structure of MOFs imposes restrictions on the interaction of the catalyst with large molecules of pollutants, in particular, phenols. To minimize diffusion restrictions during adsorption and catalysis, mesopores and macropores are added to the MOF structure using various approaches [6]. One of these approaches is the combination of an MOF with

Abbreviations and notation: MOF, metal–organic framework; SEM, scanning electron microscopy; TG, thermogravimetry; DSC, differential scanning calorimetry; XRD, X-ray diffraction analysis; BET, Brunauer–Emmett–Teller method; S_{BET} , specific surface area; S_{micro} , specific surface area of micropores, S_{ext} , specific surface area of the external surface (not involving the specific surface area of micropores); V_{tot} , total pore volume; V_{micro} , micropore volume.

porous materials to increase the degree of dispersion of the MOF [7].

In this study, it is proposed that diatomite should be used as this porous substrate material. Diatomite is a natural silica material formed by diatom shells; it has a unique structure consisting of wide meso and macropores [8]. Since diatomite is characterized by high availability, low cost, environmental safety and, at the same time, a unique developed meso–macroporous structure, it is commonly used in many branches of industry, such as agriculture [9], construction [10], and filtration [11, 12], and can be used as a base for synthesizing hierarchical composites [13–15]; in particular, it can be combined with MOFs [16].

In this context, the aim of this study is to synthesize hierarchical porous materials based on MIL-100(Fe) and diatomite, apply a new approach to synthesizing them by preimpregnating diatomite with a precursor solution, and study the structure of the resulting composite samples and the catalytic properties of MIL-100(Fe) and MIL-100(Fe)/diatomite composites in the photocatalytic degradation of phenol.

EXPERIMENTAL

Catalyst Synthesis Procedure

The samples were synthesized using diatomite (OOO Kvant, Russia) with a weight content of silica of ~90% and Al (2.53 wt %) and Fe impurities (1.81 wt %). In this study, diatomite-based composites were synthesized without acid prewashing of iron impurities from the diatomite structure, because they do not interfere with the synthesis of MIL-100(Fe); conversely, they act as a precursor for the formation of an OMPC, as shown in [17].

Solutions of iron(III) nitrate (99+%, Acros Organics) and BTC (99%, China) used to synthesize MIL-100(Fe) were taken in the following molar ratio, which was given in [18]: $1\text{Fe}(\text{NO}_3)_3 : 0.66\text{BTC} : 278\text{H}_2\text{O}$. The mixture of components was stirred at room temperature for 1 h; after that, the solution was placed in an autoclave and subjected to a hydrothermal treatment at 160°C for 12 h. The sample was washed with water and then with alcohol; after that, it was dried at 120°C for 12 h.

The composites were synthesized at the following molar ratio: $1\text{Fe}(\text{NO}_3)_3 : 0.66\text{BTC} : 6\text{SiO}_2 : 278\text{H}_2\text{O}$. The first composite was synthesized by forming MIL-100(Fe) in the presence of diatomite (MIL-100(Fe)–diatomite sample). Ten grams of diatomite were mixed with iron(III) nitrate nonahydrate (5.3 g) dissolved in 11 mL of water and BTC (1.3 g). After that, the resulting mixture was placed in an autoclave and subjected to a hydrothermal treatment at 160°C for 12 h.

To provide a better incorporation of MIL-100(Fe) into the diatomite structure, the MOF was formed directly in the diatomite pores. To synthesize this composite (MIL-100(Fe)/diatomite sample), 10 g of

diatomite was preimpregnated with a solution of iron(III) nitrate (5.3 g) by the incipient wetness impregnation method and then dried at 70°C. A BTC solution (1.3 g in 11 mL of distilled water) was added to the impregnated diatomite; the resulting mixture was placed in an autoclave and subjected to a hydrothermal treatment at 160°C for 12 h. After that, the resulting composites were washed and dried under the same conditions as those for the MIL-100(Fe) sample.

Investigation Procedures

The pore structure of the samples was studied by low-temperature nitrogen adsorption–desorption on a 3Flex specific surface area and porosity analyzer (Micromeritics, United States) with a detailed study of sorption at low relative pressures, starting from a relative pressure of the adsorbate of $P/P_0 \approx 10^{-6}$. Prior to analysis, the samples were degassed at 150°C for 5 h. Specific surface area (S_{BET}) was calculated by the Brunauer–Emmett–Teller (BET) method from the straightening of the adsorption isotherm in a relative pressure range of 0.05–0.15. Pore size distribution was determined by the Horvath–Kawazoe (micropores and narrow mesopores) and Barrett–Joyner–Halenda methods (wide mesopores). Total pore volume (V_{tot}) was calculated from nitrogen adsorption at $P/P_0 \approx 0.995$. The specific surface area and volume of micropores were determined using the comparative t -plot method.

The phase composition of the samples was studied by X-ray diffraction (XRD) analysis on an XRD-7000 diffractometer (Shimadzu, Japan) using CuK_α radiation ($\lambda = 1.54 \text{ \AA}$) in an angular range of $2\theta = 10^\circ\text{--}80^\circ$ with supplementary recording in an angular range of $2\theta = 2^\circ\text{--}16^\circ$.

The thermal stability of the samples was studied by simultaneous thermal analysis (thermogravimetry (TG) and differential scanning calorimetry (DSC)) on an STA 449 F1 Jupiter analyzer (NETZSCH, Germany). The samples were placed in a corundum crucible and treated in an air atmosphere ($v_{\text{air}} = 80 \text{ mL/min}$, $v_{\text{Ar}} = 20 \text{ mL/min}$) in a temperature range of 25–750°C at a heating rate of 10 deg/min.

The chemical composition of the surface of the samples was studied by attenuated total reflectance Fourier transform infrared spectroscopy in the fundamental absorption region ($400\text{--}4000 \text{ cm}^{-1}$) on a Nicolet 6700 instrument (Thermo Fisher Scientific, United States).

The surface morphology of the samples was studied by scanning electron microscopy (SEM) on a TM3000 scanning electron microscope (Hitachi, Japan) at an accelerating voltage of 15 kV in the sample charge elimination mode.

The catalytic properties of the synthesized samples were tested in the phenol degradation reaction in an

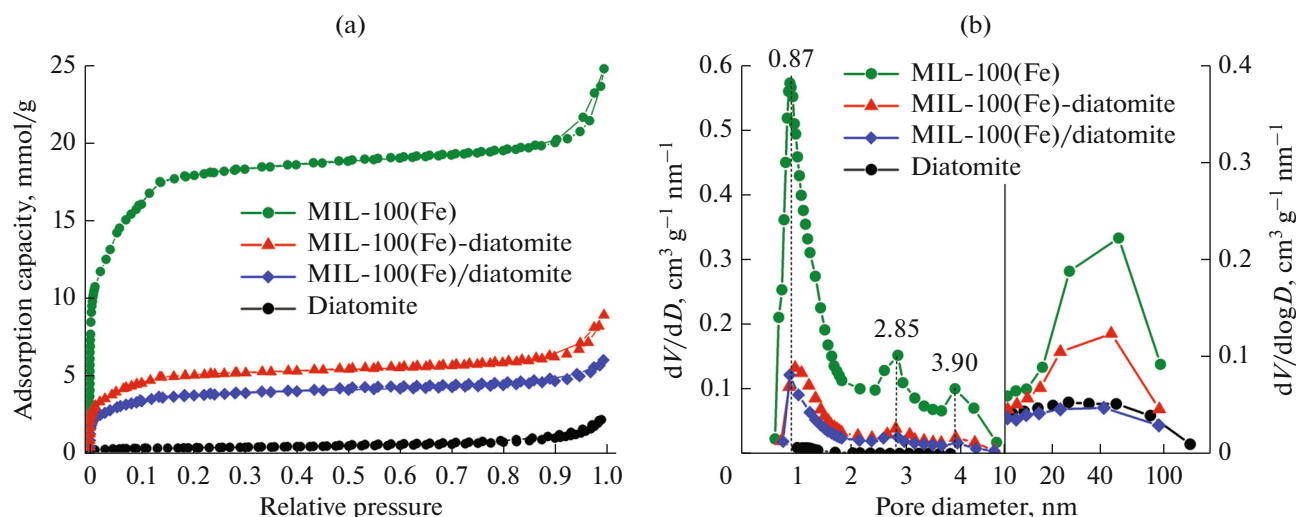


Fig. 1. (a) Low-temperature nitrogen adsorption–desorption isotherms and (b) differential pore size distribution curves for the diatomite, MIL-100(Fe), and composite samples.

aqueous solution with hydrogen peroxide in the dark and in the presence of visible radiation (photo-Fenton reaction) at 25°C, atmospheric pressure, and a stirring speed of 700 rpm. Before the catalytic test, a weighed portion of a catalyst was added to 50 mL of a phenol solution with a concentration of 25 mg/L; the mixture was stirred on a magnetic stirrer in the dark for 1 h to provide the establishment of the adsorption–desorption equilibrium. The weight of the weighed portions of the MIL-100(Fe), MIL-100(Fe)–diatomite, and MIL-100(Fe)/diatomite catalysts was 20, 60, and 100 mg, respectively. With these weighed portions, the amount of MIL-100(Fe) involved in the photocatalytic process is ~20 mg for all the catalysts. Next, an aliquot of an aqueous solution of hydrogen peroxide was added under constant stirring; the solution was subjected to irradiation for 3 h. To study the effect of the amount of hydrogen peroxide additives on the degradation level, the phenol : peroxide molar ratio was varied: it was 1 : 1, 1 : 3, 1 : 10, and 1 : 100. A Mastercolor CDM T 70W/942 G12 lamp (PHILIPS; 70 W; 0.98 A; luminous flux, 6200 lm) with a wavelength range of 340–800 nm was used as the radiation source. The phenol consumption kinetics was studied using a CM2203 spectrofluorimeter (Solar, Belarus) in a wavelength range of 270–380 nm (phenol fluorescence band at 300 nm) at an excitation wavelength of 280 nm; the slit size was 2 nm.

RESULTS AND DISCUSSION

Structure of Original Samples

The pore structure of the samples was studied by the low-temperature nitrogen adsorption–desorption method. Figure 1a shows nitrogen adsorption–desorption isotherms for the original diatomite and the synthesized MIL-100(Fe) and composite samples.

For the diatomite, an isotherm characteristic of a meso–macroporous sample with low specific surface area values is observed. The ascending of the isotherm in a relative pressures range of 0.9–1.0 suggests that wide mesopores and macropores are dominant in the sample structure. The pore size distribution (Fig. 1b) shows the presence of pores with a diameter of 10–150 nm in the sample structure; in addition, the sample can contain larger macropores, which cannot be detected by the low-temperature nitrogen adsorption method.

The isotherm for MIL-100(Fe) shows a significant increase in the adsorption capacity in the low relative pressure range; the isotherm slightly ascends at relative pressures above 0.9. This fact suggests that the pore structure of MIL-100(Fe) is mostly represented by micropores and narrow mesopores (Fig. 1b) and by wide meso- and macropores formed between the MIL-100(Fe) particles [19].

The general shapes of the isotherms (Fig. 1a) and micropore size distributions (Fig. 1b) for the composites are similar to those for the MIL-100(Fe) sample; this fact confirms the formation of MIL-100(Fe) particles on the diatomite surface. The size distribution of wide pores (Fig. 1b) shows that the MIL-100(Fe)–diatomite composite is characterized by an increase in the fraction of wide pores; at the same time, the pore size distribution curve is identical to that for the MIL-100(Fe) sample. This fact indicates the formation of MIL-100(Fe) crystallites outside the diatomite structure and the appearance of a respective number of extra wide pores between the formed particles. For the MIL-100(Fe)/diatomite composite synthesized with the preintroduction of an iron precursor directly into the porous space of the diatomite, the behavior of the mesopore size distribution curve is the same as that of the distribution curve for the original diatomite. This

Table 1. Textural characteristics of the samples

Sample	S_{BET} , m ² /g	S_{micro} , m ² /g	S_{ext} , m ² /g	V_{tot} , cm ³ /g	V_{micro} , cm ³ /g
Diatomite	31	—	31	0.05	—
MIL-100(Fe)	1570	1499	71	0.85	0.61
MIL-100(Fe)–diatomite	441	393	47	0.31	0.16
MIL-100(Fe)/diatomite	322	288	34	0.21	0.12

Dashes mean that the fraction of micropores in the sample is negligibly small.

finding suggests that the MIL-100(Fe) particles are formed directly inside the diatomite pores, rather than on the external surface of the diatomite.

Table 1 shows the textural characteristics of the samples. Diatomite has a specific surface area of 31 m²/g and a total pore volume of 0.05 cm³/g. For the MIL-100(Fe) sample, the specific surface area and pore volume values are extremely high: 1570 m²/g and 0.85 cm³/g, respectively, which is typical for MOFs. After the formation of MIL-100(Fe) on the diatomite surface, the specific surface area and pore volume values significantly increase; the increase is particularly pronounced for the MIL-100(Fe)–diatomite composite ($S_{\text{BET}} = 441$ m²/g, $V_{\text{pore}} = 0.31$ cm³/g). In the case of the composites, the contribution of micropores to the total pore volume and specific surface area is substantially smaller than that for MIL-100(Fe), because the contribution of diatomite mesopores to the overall pore structure is significant for the composites.

Thus, based on the low-temperature nitrogen adsorption–desorption data, it can be concluded that the synthesis of the composites leads to the formation of MIL-100(Fe) particles; however, their distribution on the diatomite surface depends on the chosen syn-

thesis approach: for the first composite, MIL-100(Fe) particles are formed mostly on the external surface of the diatomite, whereas for the second composite synthesized with the preimpregnation of diatomite with iron salts, it is reasonable to expect the formation of MIL-100(Fe) particles directly in the porous space of the diatomite. The composites are characterized by a hierarchical pore structure represented by micropores and narrow mesopores of the resulting MIL-100(Fe) particles and by wide meso- and macropores that are present in the original diatomite and/or formed due to the aggregation of MIL-100(Fe) particles.

The phase composition of the samples was studied by XRD analysis (Fig. 2). In a region of $2\theta = 17^\circ$ – 26° , the diffraction pattern of diatomite exhibits a broad halo, which is attributed to the main phase of diatomite, i.e., amorphous SiO₂. The intense reflections at $2\theta = 21^\circ$ and 27° correspond to the crystalline α -quartz phase. For the MIL-100(Fe) sample, in a region of $2\theta = 2^\circ$ – 16° (Fig. 2a), the diffraction pattern exhibits reflections that, according to [20], are characteristic of the MIL-100(Fe) MOF; this fact confirms the formation of the MIL-100(Fe) structure.

In an angular range of $2\theta = 16^\circ$ – 40° (Fig. 2b), the diffraction patterns of the composites exhibit reflec-

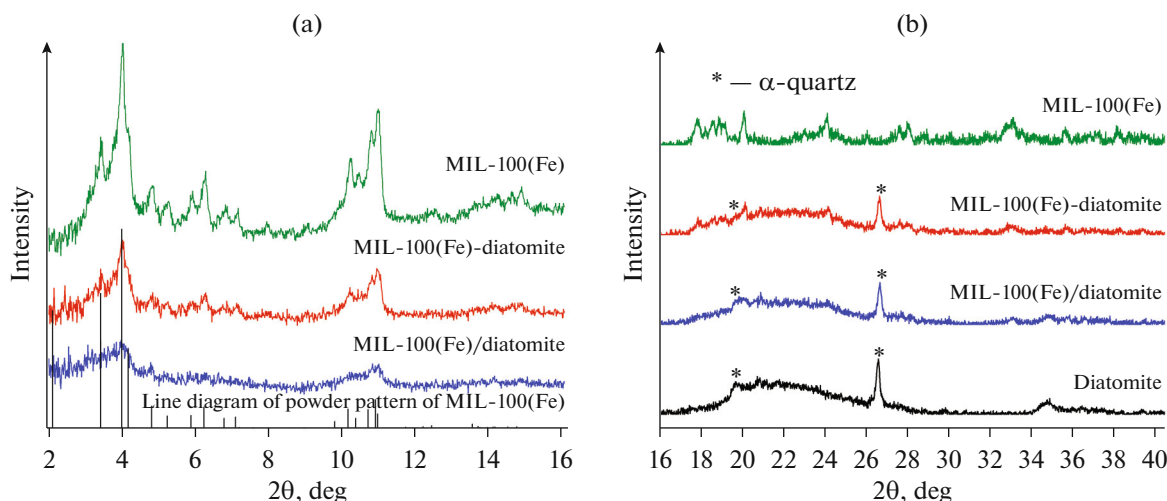


Fig. 2. Diffraction patterns of the studied samples in an angular range of (a) $2\theta = 2^\circ$ – 16° and (b) 16° – 40° .

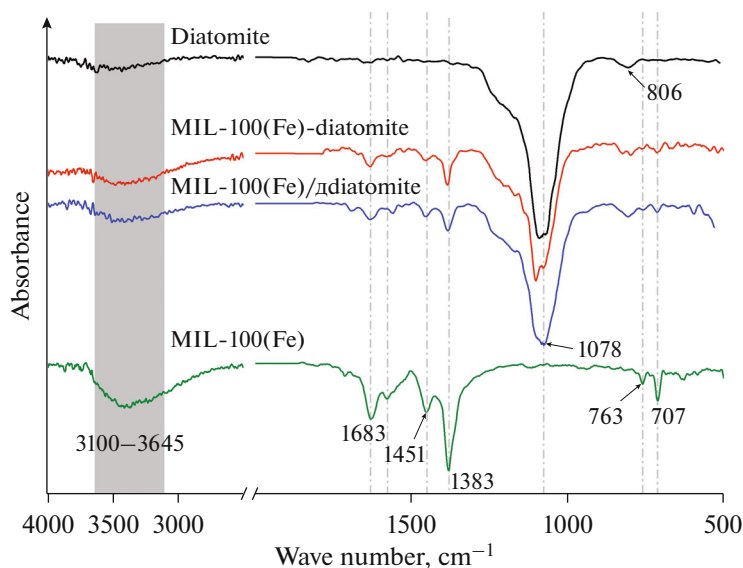


Fig. 3. Infrared spectra of the studied samples.

tions attributed to both the original diatomite and MIL-100(Fe). In the region of small angles, reflections corresponding to MIL-100(Fe) are identified more reliably; this fact indicates the formation of crystallites with a MIL-100(Fe) structure on the diatomite surface. A decrease in the intensity of these reflections and their broadening for the composites indicates the formation of smaller MIL-100(Fe) particles. At the same time, in the diffraction pattern in an angular range of $2\theta = 2^\circ\text{--}16^\circ$ (Fig. 2a), the intensity of the reflections corresponding to the MIL-100(Fe) phase for the MIL-100(Fe)–diatomite sample is higher than that for MIL-100(Fe)/diatomite. This fact can indicate the presence of larger MIL-100(Fe) crystallites in the MIL-100(Fe)–diatomite composite; the growth of these crystallites on the external surface of the diatomite is more probable than their growth inside the diatomite pores. Thus, both diatomite and formed MOF particles with a MIL-100(Fe) structure are present in the synthesized composites. At the same time, the deposition method determines the MIL-100(Fe) particle size in the composites. Preimpregnation provides the formation of smaller MIL-100(Fe) particles on the diatomite surface.

Figure 3 shows IR spectra of the studied samples. The spectra of diatomite exhibit absorption bands corresponding to the asymmetric vibrations of Si–O–Si bonds (1078 cm^{-1}) and the stretching vibrations of Al–O–Si (806 cm^{-1}); these data are consistent with the IR spectra of diatomite given in [21]. The spectrum of MIL-100(Fe) exhibits absorption bands attributed to the stretching vibrations of the C=O bond in carboxyl groups (1683 cm^{-1}) and the symmetric and asymmetric vibrations of the –O–C–O group (1451 and 1383 cm^{-1}). The broad band at $\sim 3100\text{--}3645\text{ cm}^{-1}$ is attributed to

the stretching vibrations of the –OH group of physically adsorbed water contained in the MIL-100(Fe) pores. The bands at 763 and 707 cm^{-1} correspond to the bending vibrations of the C–H bonds of the benzene ring [22]. The presence of absorption bands characteristic of both MIL-100(Fe) and diatomite in the IR spectra of the composites confirms the formation of an MOF on the diatomite surface.

The thermal stability of the synthesized samples was studied by TG analysis in an oxidizing environment (Fig. 4). For all the samples, in a temperature range of $50\text{--}150^\circ\text{C}$, a weight loss associated with the removal of physically adsorbed water is observed. In a range of $150\text{--}250^\circ\text{C}$, the exothermic removal of chemisorbed water takes place. The weight loss steps in a range of $300\text{--}450^\circ\text{C}$, which are typical for all the samples, correspond to the exothermic oxidative degradation of the organic component of MIL-100(Fe) to CO_2 and H_2O [23]. This process leads to the degradation of the MOF structure to Fe_2O_3 (residual weight of 30.19%). For MIL-100(Fe)–diatomite and MIL-100(Fe)/diatomite, due to the presence of silica in the structure, the residual weight is 72.81 and 81.14%, respectively. Data on weight loss in a range of $300\text{--}450^\circ\text{C}$ can be used to calculate the amount of the MOF in the samples; in the MIL-100(Fe)–diatomite and MIL-100(Fe)/diatomite composites, it is ~ 31.12 and $\sim 23.42\%$, respectively. The iron content in the composites is 8.50 and 5.74 wt %, respectively. Thus, based on the simultaneous thermal analysis data, it can be concluded that the composite structure contains particles of the MIL-100(Fe) material and the synthesized composites are stable in an oxidizing environment up to a temperature of $\sim 300^\circ\text{C}$.

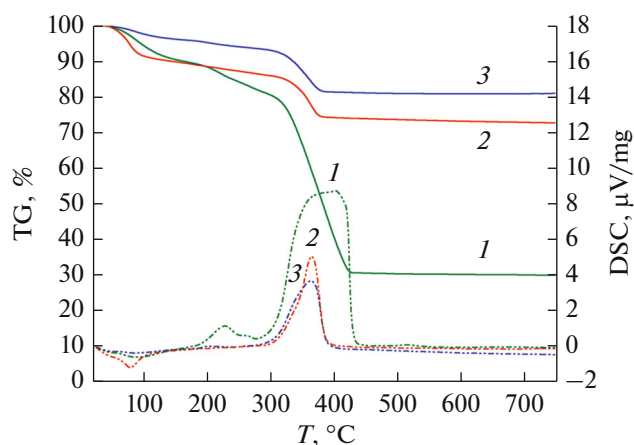


Fig. 4. (solid lines) Thermogravimetry curves and (dashed lines) DSC curves for (1) MIL-100(Fe), (2) MIL-100(Fe)–diatomite, and (3) MIL-100(Fe)/diatomite.

Figure 5 shows SEM images of the studied samples. It is evident that diatomite contains remains of diatom shells (Fig. 5a): large fragments with a preserved

porous structure, smaller fragments, and small pieces, for which the uniqueness of the structure is poorly visible. According to SEM, diatomite has a meso–macroporous structure with pores ranging in size from 90 nm to 2 μm . The SEM image of MIL-100(Fe) shows large irregularly shaped particles, which are agglomerates formed due to the coalescence of MIL-100(Fe) particles (Fig. 5b).

For the composites (Figs. 5c, 5d), the presence of remains of diatom shells is observed; this fact indicates the preservation of the porous structure of diatomite. The absence of large irregularly shaped particles characteristic of MIL-100(Fe) (as in Fig. 5b) indirectly confirms that MIL-100(Fe) is quite uniformly distributed over the surface. For the MIL-100(Fe)–diatomite composite (Fig. 5c), diatom shell fragments are less distinguishable on SEM images; particles without a pronounced diatomite structure are present; they can be assigned to MIL-100(Fe), because they are similar to the particles shown in Fig. 5b. For the MIL-100(Fe)/diatomite composite, a significant number of particles with a pronounced diatomite structure are visible; the number of small shapeless

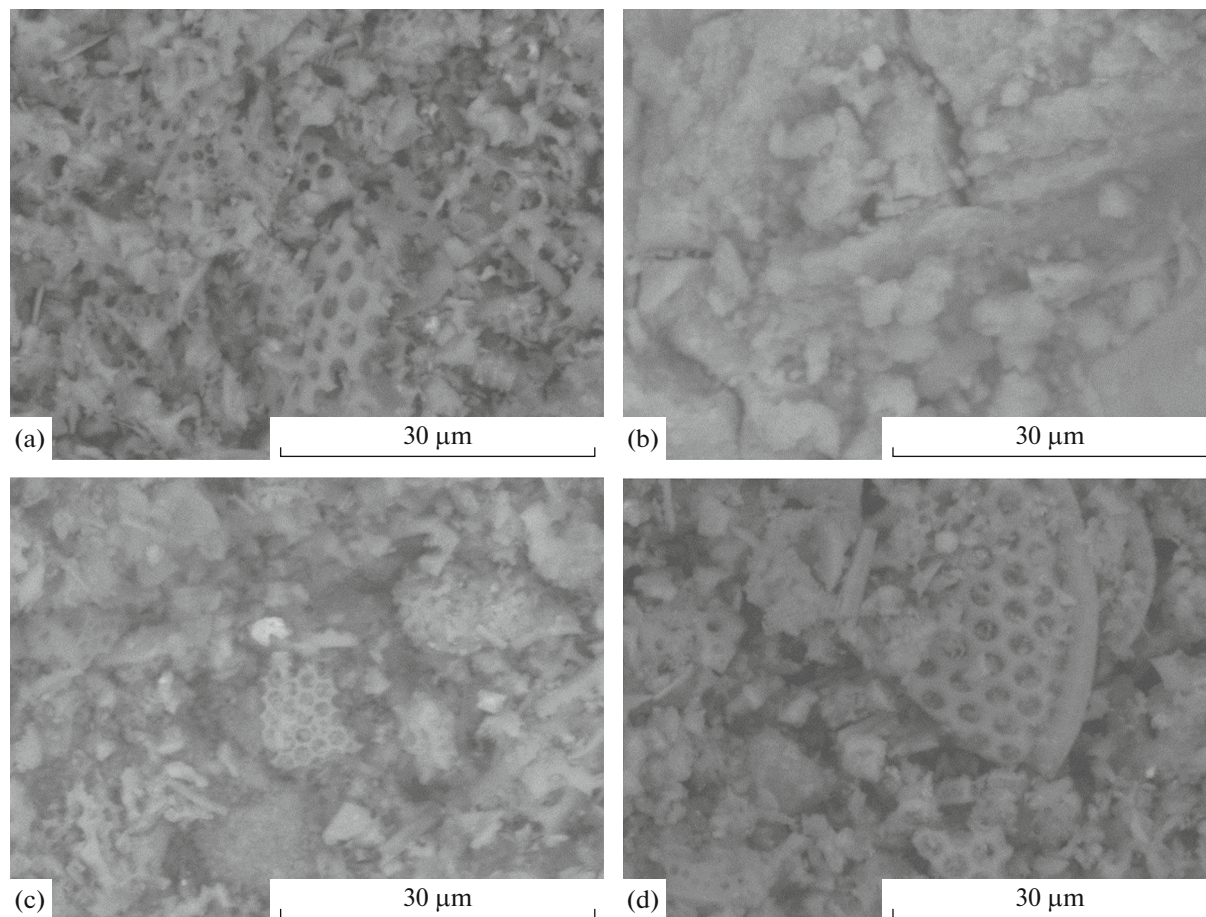


Fig. 5. Scanning electron microscopy images of (a) diatomite, (b) MIL-100(Fe), (c) MIL-100(Fe)–diatomite, and (d) MIL-100(Fe)/diatomite.

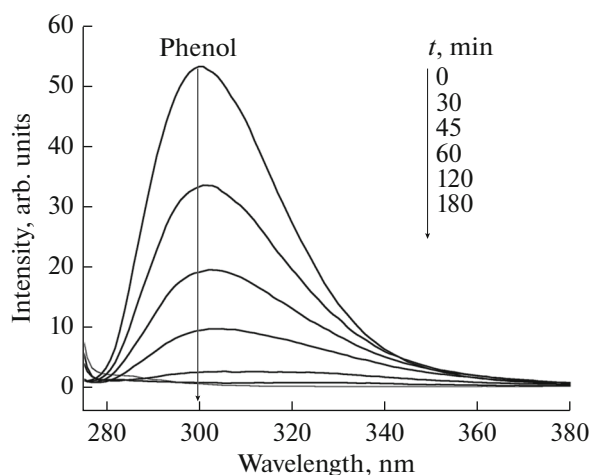


Fig. 6. Fluorescence spectra of phenol in the presence of MIL-100(Fe) under the action of light at a phenol : H₂O₂ ratio of 1 : 10.

particles is less. These results are consistent with the nitrogen adsorption and XRD data on the formation of larger MIL-100(Fe) particles in the structure of the MIL-100(Fe)–diatomite composite, which are distributed outside the diatomite structure, and on the formation of smaller MIL-100(Fe) particles localized directly in the diatomite pores.

Phenol Degradation

The catalytic properties of the synthesized samples were studied in the phenol degradation reaction in an aqueous solution in the presence of hydrogen peroxide. The occurrence of the reaction was monitored from the change in the intensity of the fluorescence

spectrum of phenol at an emission wavelength of 300 nm (Fig. 6).

Figure 7a shows the kinetic curves of the dependence of the phenol fluorescence intensity under varying conditions. Upon the addition of hydrogen peroxide and illumination for 180 min, the phenol concentration hardly changes at all. A pronounced degradation of phenol is observed only after the introduction of hydrogen peroxide and MIL-100(Fe) into the system. In the phenol/H₂O₂/light, phenol/MIL-100(Fe)/darkness, and phenol/MIL-100(Fe)/light systems, 15–20% of the entire phenol undergo degradation. It is evident from the data that the reaction occurs faster in the presence of light; this fact indicates the occurrence of the photo-Fenton process.

Figure 7b shows the kinetic curves of phenol degradation in the presence of MIL-100(Fe) at the different phenol : H₂O₂ ratios under the action of visible radiation. At a phenol : H₂O₂ ratio of 1 : 1 and 1 : 3, within 180 min, 50 and 90% of the entire phenol, respectively, undergo degradation. At ratios of 1 : 10 and 1 : 20, phenol undergoes complete degradation within ~120 min. For the reaction that occurs at a phenol : H₂O₂ ratio of 1 : 100, complete degradation is achieved within 160 min. The observed dependence can be associated with the fact that, with an increase in the hydrogen peroxide concentration, the degradation rate of phenol increases. In the presence of a large amount of excess H₂O₂ (ratio of 1 : 100), the reaction slows down due to the interaction of a large number of OH[•] radicals with H₂O₂ to form less active radicals (reactions (I) and (II)) [24]:

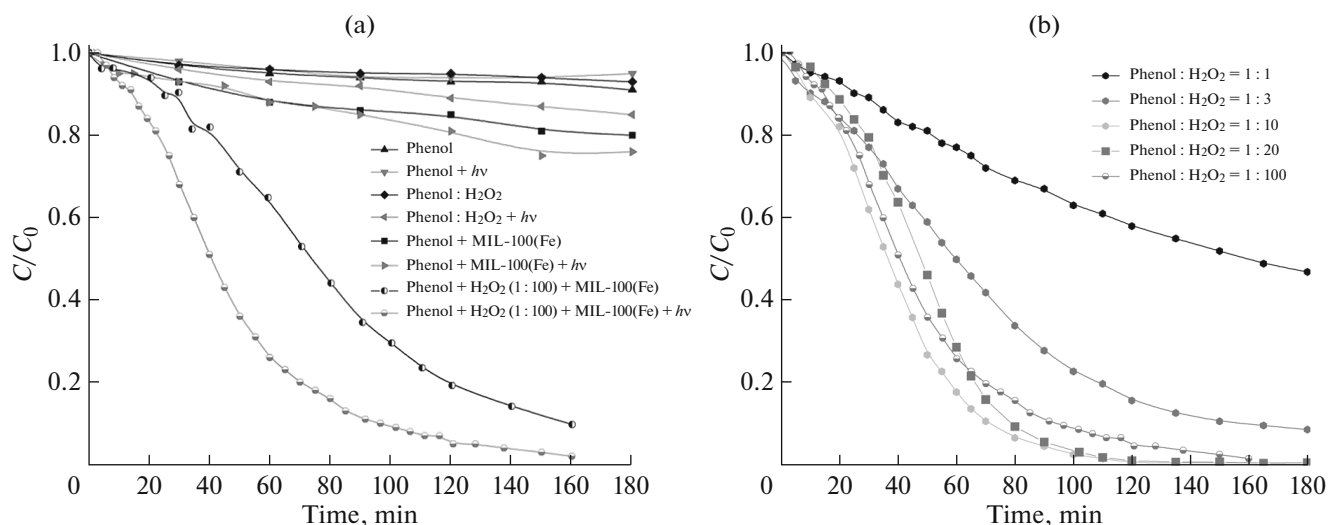
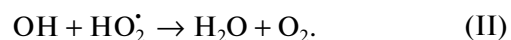
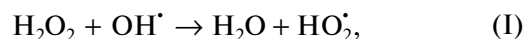


Fig. 7. Kinetic curves recorded in (a) blank tests and (b) tests with a variation in the phenol : H₂O₂ ratio under the action of visible radiation in the phenol degradation reaction in the presence of MIL-100(Fe).

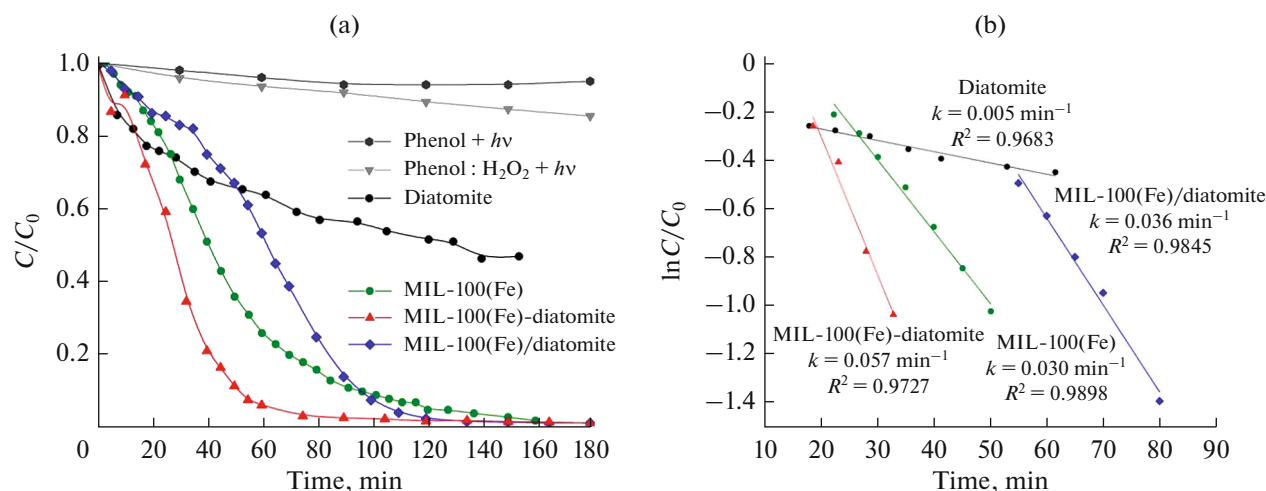
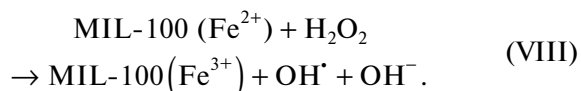
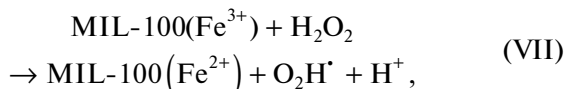
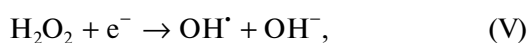


Fig. 8. (a) Kinetic curves of the photocatalytic oxidation of phenol at a phenol : H_2O_2 ratio of 1 : 100 and (b) results of straightening the kinetic curves in the first-order reaction coordinates.

The proposed mechanism of the formation of radicals involved in phenol oxidation is represented by the following reactions:



The irradiation of a heterogeneous photocatalyst leads to the formation of photogenerated electrons and holes (reactions (III), (IV)). Electrons gradually accumulate on the Fe–MOF surface and activate H_2O_2 and a small amount of O_2 to form respective radicals (reactions (V), (VI)). Iron ions on the MOF surface can also directly activate H_2O_2 to form OH^\cdot radicals (reactions (VII), (VIII)). Due to the high oxidation potential, the resulting radicals interact with the pollutant to degrade it to oxidation products [2, 25–27].

The synthesized catalysts were compared in terms of activity in the sample/phenol/ H_2O_2 /light system (Fig. 8a). The phenol : H_2O_2 ratio of 1 : 100 was used to linearize the recorded kinetic curves in pseudo-first-order coordinates (Fig. 8b). The original diatomite is characterized by low activity in the studied reaction: ~50% of the entire phenol undergoes degradation within 160 min; this fact is attributed to the

presence of a small amount of iron in the diatomite structure. All the kinetic curves exhibit an induction period varying in a range of 15–50 min. According to [28], iron on the MIL-100(Fe) surface is in the Fe(III) state. Therefore, the induction period is associated with the transition of Fe(III) to the Fe(II) state, which is necessary for the further occurrence of reaction (IV) [29–31].

The values of the constants listed in Table 2 show that the composites exhibit a higher catalytic activity in the photocatalytic degradation of phenol than the activity of MIL-100(Fe). Thus, for the MIL-100(Fe)–diatomite sample, the phenol degradation rate constant is 0.057 min^{-1} ; for the MIL-100(Fe)/diatomite sample, $k = 0.036 \text{ min}^{-1}$. This fact can be attributed to the highly dispersed state of the MIL-100(Fe) particles formed on the diatomite surface in the composites and, therefore, their high accessibility to the catalytic process. Since the catalytic tests were conducted so that to provide an identical amount of iron in the samples, the ratio of the reaction rate constant to the weight of iron (k/m quantity in Table 2) is a measure that characterizes the accessibility and activity of the Fe-containing catalyst sites. The highest activity is observed for the MIL-100(Fe)–diatomite catalyst. This fact can be attributed to the formation of small MOF crystallites and their localization on the external side of the diatomite, which makes the respective Fe-containing sites more accessible to reagents due to a decrease in the diffusion hindrances inside the microporous MOF crystallites [34].

The data on the activity of the catalysts used in this study are comparable to the data for other samples based on MOFs, which are given in Table 2. This fact confirms that the choice of the composites as photo-

Table 2. Catalytic properties of the samples

Sample	Phenol : H ₂ O ₂ ratio	m_{cat} , mg	t_{degr} , min	k , min ⁻¹	k/m^* , min ⁻¹ g ⁻¹	References
Diatomite	1 : 100	20	—	0.005	—	This study
MIL-100(Fe)	1 : 100	20	160	0.030	6.4	
MIL-100(Fe)/diatomite	1 : 100	100	120	0.036	6.3	
MIL-100(Fe)—diatomite	1 : 100	60	85	0.057	11.2	
PDI/MIL-88A	1 : 6	15	60	0.077	—	[32]
MIL-100(Fe)/ZnO	1 : 188	10	120	0.034	—	[33]

* k/m is the reaction rate constant related to the weight of MIL-100(Fe). Dashes indicate the unavailability of data.

catalysts for phenol oxidation in the presence of hydrogen peroxide is justified.

CONCLUSIONS

The composites based on diatomite and the MIL-100(Fe) MOF are characterized by a hierarchical macro–meso–microporous structure. The MIL-100(Fe) MOF is distributed both on the external surface and inside the pores of the diatomite. The synthesized samples exhibit high activity in the phenol degradation reaction in aqueous solutions both in the dark and in the light. Under irradiation with light, phenol undergoes degradation faster; this fact is attributed to the contribution of photocatalytic processes. The activity of the samples synthesized in this study and the known photocatalysts varies within one order of magnitude. The highest activity is exhibited by the MIL-100(Fe)—diatomite composite, which is a mixture of diatomite and MIL-100(Fe) particles. The fact that it exhibits a higher activity than that of the bulk MIL-100(Fe) sample can be associated primarily with the smaller size of the MOF particles due to their stabilization on the diatomite surface.

ACKNOWLEDGMENTS

The authors thank L.A. Selyunina (Faculty of Chemistry, National Research Tomsk State University) for conducting SEM studies.

FUNDING

This work was supported by the Russian Foundation for Basic Research and the Administration of the Tomsk oblast within the framework of research project no. 19-43-700008 r_a.

CONFLICT OF INTEREST

The authors declare that they have no conflict of interest.

REFERENCES

- Busca, G., Berardinelli, S., Resini, C., and Arrighi, L., *J. Hazard. Mater.*, 2008, vol. 160, nos. 2–3, p. 265.
- Clarizia, L., Russo, D., Di Somma, I., Marotta, R., and Andreozzi, R., *Appl. Catal. B: Environ.*, 2017, vol. 209, p. 358.
- Sashkina, K.A., Semeikina, V.S., Labko, V.S., Rudina, N.A., and Parkhomchuk, E.V., *Kinet. Katal.*, 2013, vol. 54, no. 5, p. 676.
- Nivetha, R., Gothandapani, K., Raghavan, V., Jacob, G., Sellappan, R., Bhardwaj, P., Pitchaimuthu, S., Kannan, A.N.M., Jeong, S.K., and Grace, N., *ACS Omega*, 2020, vol. 5, no. 30, p. 18941.
- Wang, S. and Wang, X., *Small*, 2015, vol. 11, no. 26, p. 3097.
- Cai, G., Yan, P., Zhang, L., Zhou, H.C., and Jiang, H.L., *Chem. Rev.*, 2021, vol. 121, no. 20, p. 12278.
- Isaeva, V.I., Chernyshev, V.V., and Fomkin, A.A., *Micropor. Mesopor. Mater.*, 2020, vol. 300, p. 110136.
- Engh, K.R., Diatomite, in *Kirk-Othmer Encyclopedia of Chemical Technology*, Hoboken, NJ: Wiley, 2000.
- Kapranov, V.N. and Kamskii, A.V., *Plododorodie*, 2006, vol. 31, no. 4, p. 12.
- Yılmaz, B. and Ediz, N., *Cem. Concr. Compos.*, 2008, vol. 30, no. 3, p. 202.
- Millqvist, M.T. and Luz, A.B., *Mining Metall. Explor.*, 2003, vol. 20, no. 1, p. 42.
- Ghobara, M. and Mohamed, A., in *Diatoms: Fundamentals and Applications*, Gordon, R. and Seckbach, J., Eds., Hoboken, NJ: Wiley and Salem, 2019, p. 471.
- Liu, D., Gu, J., Liu, Q., and Tan, Y., Li, Z., Zhang, W., Su, Y., Li, W., Cui, A., Gu, C., and Zhang, D., *Adv. Mater.*, 2014, vol. 26, no. 8, p. 1229.
- Zubkov, A.V., Vyshegorodtseva, E.V., Bugrova, T.A., and Mamontov, G.V., *J. Phys. Conf. Ser.*, 2020, vol. 1611, no. 1, p. 012040.
- Mamontov, G.V., RF Patent 2727393, 2020.
- Evdokimova, E.V., Matskan, P.A., and Mamontov, G.V., *Zh. Fiz. Khim.*, 2022, vol. 96, no. 1, p. 107.

17. Vyshegorodtseva, E.V., Matskan, P.A., and Mamonov, G.V., *AIP Conf. Proc.*, 2020, vol. 2301, no. 1, p. 040018.
18. Seo, Y., Yoon, J.W., Lee, J.S., Lee, H., Hwang, Y.K., Jun, H., Horcajada, P., Serre, C., and Chang, S., *Micropor. Mesopor. Mater.*, 2012, vol. 157, p. 137.
19. Atyaksheva, L.F., Dobryakova, I.V., Ivanova, I.I., and Knyazeva E.E., *Russ. J. Phys. Chem. A*, 2015, vol. 89, no. 10, p. 1924.
20. Simon, M.A., Anggraeni, E., Soetaredjo, F.E., Santoso, S.P., Irawaty, W., Thanh, T.C., Hartono, S.B., Yuliana, M., and Ismadji, S., *Sci. Rep.*, vol. 9, no. 1, p. 1.
21. Uthappa, U.T., Kigga, M., Sriram, G., Ajeya, K.V., Jung, H.Y., Neelgund, G.M., and Kurkuri, M.D., *Micropor. Mesopor. Mater.*, 2019, vol. 288, p. 109572.
22. Nehra, M., Dilbaghi, N., Singhal, N.K., Hassan, A., Kim, K., and Kumar, S., *Environ. Res.*, 2019, vol. 169, p. 229.
23. Chen, C., Li, B., Zhou, L., Xia, Z., Feng, N., Ding, J., Wang, L., Wan, H., and Guan, G., *ACS Appl. Mater. Interfaces*, 2017, vol. 9, no. 27, p. 23060.
24. Herney-Ramirez, J., Vicente, M.A., and Madeira, L.M., *Appl. Catal. B: Environ.*, 2010, vol. 98, nos. 1–2, p. 10.
25. Ameta R., Chohadia A.K., Jain A., and Punjabi, P.B., in *Advanced Oxidation Processes for Waste Water Treatment*, Ameta, S.C. and Ameta, R., Eds., Cambridge, MA: Academic Press, 2018, p. 49.
26. Du, C., Zhang, Y., Zhang, Z., Zhou, L., Yu, G., Wen, X., Chi, T., Wang, G., Su, Y., Deng, F., Lv, Y., and Zhu, H., *Chem. Eng. J.*, 2022, vol. 431, p. 133932.
27. Mohammadifard, Z., Saboori, R., Mirbagheri, N.S., and Sabbaghi, S., *Environ. Pollut.*, 2019, vol. 251, p. 783.
28. Lv, H., Zhao, H., Cao, T., Qian, L., Wang, Y., and Zhao, G., *J. Mol. Catal. A. Chem.*, 2015, vol. 400, p. 81.
29. Wu, K., Xie, Y., Zhao, J., and Hidaka, H., *J. Mol. Catal. A. Chem.*, 1999, vol. 144, no. 1, p. 77.
30. Luo, M., Bowden, D., and Brimblecombe, P., *Appl. Catal. B: Environ.*, 2009, vol. 85, nos. 3–4, p. 201.
31. Chellal, K., Bachari, K., and Sadi, F., *Kinet. Catal.*, 2014, vol. 55, no. 4, p. 467.
32. Huang, W., Shao, H., Song, M., Yang, Z., and Liao, X., *Appl. Surf. Sci.*, 2021, vol. 547, p. 149222.
33. Ahmad, M., Chen, S., Ye, F., Quan, X., Afzal, S., Yu, H., and Zhao, X., *Appl. Catal. B: Environ.*, 2019, vol. 245, p. 428.
34. Dhakshinamoorthy, A., Alvaro, M., Hwang, Y.K., Seo, Y.K., Corma, A., and Garcia, H., *Dalton Transact.*, 2011, vol. 40, no. 40, p. 10719.

Translated by M. Timoshinina